Materials Science-Poland, 39(3), 2021, pp. 410-429
http://www.materialsscience.pwr.wroc.pl/
DOI: 10.2478/msp-2021-0033

sciendo

The influence of ball milling processing variables on the microstructure and compaction behavior of Fe–Mn–Cu alloys

Hany R. Ammar[1,2,*], Subbarayan Sivasankaran[1], Abdulaziz S. Alaboodi[1]

[1]Department of Mechanical Engineering, College of Engineering, Qassim University, Buraydah 51452, Saudi Arabia
[2]Metallurgical and Materials Engineering Department, Faculty of Petroleum and Mining Engineering, Suez University, Suez 43511, Egypt

In the present study, twenty seven [$(Fe–35wt\%Mn)_{100-x}–Cu_x$] alloy samples were processed using high-energy ball milling, followed by uniaxial compaction under different processing conditions. The compressibility behavior in terms of relative density (RD) was examined with milling time (MT: 1 h, 5.5 h, and 10 h), ball-to-powder mass ratio (BPMR: 5:1, 10:1, and 15:1), milling speed (MS: 100 rev/min, 200 rev/min, and 300 rev/min), compaction pressure (CP: 25–1,100 MPa), and alloy composition (Cu content [CC]: 0 wt%, 5 wt%, 10 wt%). Particle size analysis using X-ray diffraction (XRD) and high-resolution scanning electron microscopy (HRSEM) combined with energy-dispersive X-ray spectroscopy (EDS) were applied for microstructural characterization. The experiments were conducted based on the central composite design of response surface methodology (RSM), and the results for the compaction behavior were examined with the input parameters. Analysis of variance (ANOVA) test was applied to determine the most significant input parameters. The attained results revealed that increasing ball milling parameters (MT, MS, and BPMR) resulted in significant enhancements in the microstructural features, such as improved elemental dispersion and occurrence of refined particles with substantial decrease in the crystallite size. On the other hand, increasing the input parameters exhibited a detrimental influence on the compactibility and RD of the alloys. In addition, increasing the CC resulted in a substantial improvement in the compressibility and RD of the developed alloys. The recommended combination of the studied variables includes MT for 5 h, MS for 150 rev/min, BPMR of 10:1, and 10 wt%Cu to attain an acceptable compromise of enhanced microstructure features, improved compaction response, and RD.

Keywords: *ball milling, Fe–Mn–Cu alloys, microstructure, compaction behavior, relative density, ANOVA*

1. Introduction

High-energy ball milling/mechanical alloying is used for producing a wide range of engineering materials due to several advantages, such as synthesis of homogeneous nanostructured materials [1], composite materials [2], metallic solid solutions [3], and intermetallics [4]. Ball milling displays a significant advantage in terms of alloying immiscible elements [5] and forming stable and metastable phases [6]. Several techniques are available for material processing, among which solid-state processing using ball milling plays a major role; this process can be used to manufacture nanomaterials on a large industrial scale [7]. The strength, hardness, and electrical conductivity of Al–Cu composites were significantly improved by a new production technique that involved ball milling and microwave sintering. The sintered samples were post-treated using friction stir process [8]. Based on the materials' application requirements, the materials synthesized via ball milling displayed various structures, such as supersaturated, nanocrystalline [9], and homogeneous amorphous [10] forms. Milling maps were generated based on the milling conditions to define the boundaries of the formed phases, either crystalline or amorphous [11]. Powder metallurgy (P/M) is widely used for fabricating several metal-based products for many engineering applications [12]; fabricating net-shaped complex parts is an attractive feature of the P/M method [13]. Ball milling, however, requires careful selection of the processing variables that affect the synthesized materials' structure and performance. These processing variables, which include the milling time (MT), ball-to-powder mass ratio (BPMR), milling

* E-mail: hanyammar@qec.edu.sa

© 2021. This is an open access article distributed under the Creative Commons Attribution-NonCommercial-NoDerivatives 4.0 License.
(http://creativecommons.org/licenses/by-nc-nd/4.0/)

speed (MS), grinding medium (GM), and milling atmosphere (MAT), influence the performance of the material. Optimum selection of these processing variables is critical to attain the desired structure/performance of the produced materials [1].

Fe–Mn–Cu alloys are used as biodegradable materials (BDMs). These materials are used for supporting a treated tissue during the healing period and, thereafter, they degrade progressively without leaving behind any implant material; consequently, the recovery course can be completed without additional medical action [14]. Fe–Mn–Cu alloys have been designed as BDMs for medical applications, including fracture fixation and temporary orthopedic devices [15], cardiovascular support and other devices [16], and stent implantation [17]. The basic requirements of BDMs are compatibility, rigidity, acceptable strength, and high rate of degradation [18]. Therefore, metallic materials, such as iron (Fe), magnesium (Mg), zinc (Zn), and their alloys, are used as BDMs [19]. Fe-based alloys are favorable BDMs, due to their high strength and stiffness; these alloys also display a low rate of corrosion [20]. The mechanical and corrosion properties of Fe-based BDMs have been investigated in several studies. The degradation rate of Fe scaffolds was found to be accelerated by the nitriding technique [21]. Fe–Mn alloys developed for cardiovascular uses exhibited improved mechanical strength, biocompatibility, and corrosion-resistant properties [22]. Fe–hydroxyapatite composites were developed with enhanced corrosion properties; however, the obtained mechanical properties were reported to be lower than those of Fe [23]. Numerous researchers have studied the effects of the synthesis techniques used and the alloying elements added on the mechanical behavior and degradability of Fe-based alloys. The corrosion behavior of Fe–Mn–C–Pd BDMs in virtual fluids of the human body was investigated [24]. The mechanical properties and degradation behavior of Fe–Mn–C–S BDMs produced by the casting method with rapid cooling rate were examined [25]. The properties of Fe_{30}-Mn_6-Si alloy produced by the melting route were evaluated for biodegradable applications [26]. Fe–(20, 25, 30, 35)–Mn were produced by P/M for biodegradable stents [27]. The influence of alloying elements such as Mn, Co, Al, W, B, C, S, and Sn on the biocompatibility and biodegradability of Fe produced by the casting method was examined [28]. Ball milling/mechanical alloying was successfully used for synthesizing several BDMs, such as Fe–Mn–Cu [15], Fe–30Mn–(1–3)Ag [29], Fe–30 wt% Mn [30], and Fe–35 wt%Mn [31].

The study of compressibility and relative density (RD) of the processed powders before further processing is technologically significant, because the RD of the compacted samples affects not only the possibility of green sample handling for further processing but also the mechanical behavior of the final parts obtained by P/M. Several factors influence the compressibility of powders. The influence of the powder characteristics on the compressibility of Al-6061–TiO_2 micro/nanocomposites produced by low-/high-energy ball milling has been studied [32]. The compressibility of Fe powders has been observed to depend on the powder characteristics such as size and morphology [33]. The applied load, powder composition, and annealing treatment also affect the compressibility of powders [34]; the MT of mechanically alloyed powders has a significant impact on the powder's compressibility [35]. The ball milling/mechanical alloying process is probabilistic in nature, and the performance of this process depends on the proper selection of the input and output process parameters [36]. Presently, designing of experiments for minimizing the number of experiments is widely used [37].

In the present study, the effect of ball milling input parameters on the microstructure and compactibility (RD) of processed [(Fe–35wt%Mn)$_{100-x}$–Cu_x] alloy powders was examined. The parameters used in this study were MT, BPMR, MS, CP, and alloy composition (Cu content [CC]). RSM was used to analyze the mutual effect of the input parameters on the compaction behavior in terms of RD. Designing of the experiments was performed using Minitab software. In addition, analysis of variance (ANOVA) test was used to determine the most significant input parameters affecting the compressibility.

2. Materials and methods

2.1. Synthesis of [(Fe–35wt%Mn)$_{100-x}$–Cu$_x$] alloys with various input parameters

Table 1 displays the design input parameters for the present study, which includes 27 experiments conducted on the [(Fe–35wt%Mn)$_{100-x}$–Cu$_x$] system, where x = 0 wt%, 5 wt%, and 10 wt%. The processing variables comprise the MT (1 h, 5.5 h, and 10 h), BPMR (5:1, 10:1, and 15:1), and MS (100 rev/min, 200 rev/min, and 300 rev/min). Ball milling of the as-received Fe, Mn, and Cu powders, with purity >99.5% (supplied by Nanografi, Germany), was carried out using Pulverisette 5/2 classic line (Fritsch GmbH - Milling and Sizing, Idar-Oberstein, Germany) through simultaneous milling in two tungsten carbide (WC) containers (250 mL capacity each) using 10-mm-diameter balls made of tungsten carbide. The process was performed continuously to complete the MT by repeating a milling cycle comprising four stages: vial rotation in the forward path for 15 min; a stop for 15 min; vail rotation in the reverse path for 15 min; and one more stop for 15 min. The two stops in each cycle were implemented to inhibit overheating inside the milling containers. For each experiment, the as-received powders were premixed based on the designed composition and then the premixed powders were ball-milled for the designed MT, MS, and BPMR, according to the design of experiments shown in Table 1. The ball milling was conducted in a wet medium of ethanol (pureness >99.9%) to inhibit oxidization and agglomeration of the developed alloy powders.

2.2. Characterization of the microstructure of the developed [(Fe–35wt%Mn)$_{100-x}$–Cu$_x$] alloys

All processed samples were examined by X-ray diffraction (XRD) to identify the formed phases and to calculate the crystallite size and lattice strain under various processing conditions. An XRD machine (Empyrean, Malvern Panalytical) was used with a radiation source of Cu-$k\alpha$ to investigate the specimens at a rate of 0.6°/min and a step size of 0.01° with a range of 2θ from 20° to 80°. The obtained XRD data were analyzed using the X'Pert High Score Plus software for phase identification and determination of crystallite size and lattice strain. The crystallite size was calculated using the Scherer formula [Eq. (1)], based on the major Fe peak only, and the homogeneous lattice strain was determined from the ratio of the deviation of standard and calculated d-spacing in relative to the standard d-spacing [38]. The Williamson–Hall method can also be used to determine the crystallite size and lattice strain. However, here, only two major XRD peaks were observed and, hence, Scherer formula was used. Furthermore, the instrumental broadening was accounted for according to the basic equation and inbuilt in the software. The XRD machine gave the data after deducting the instrumental broadening [according to Eq. (2)]. Scherer formula [Eq. (1)] was used to determine the crystallite size as follows:

$$t = \frac{k\lambda}{\beta \cos\theta} \tag{1}$$

where t is the crystal size, λ is X-ray wavelength, θ is Bragg's angle, and β is the full-width at half-maximum. The instrumental broadening was corrected using Eq. (2) as follows:

$$\beta_{hkl} = \left[(\beta_{hkl})^2_{\text{Measured}} - (\beta_{hkl})^2_{\text{Instrumental}}\right]^{1/2} \tag{2}$$

A field-emission gun high-resolution scanning electron microscope (FEG-HR-SEM; Apreo; ThermoScientific) coupled with an energy-dispersive spectrometer (EDS) was used for investigating the microstructure of the selected samples under varying processing conditions. The size and morphology of the as-received and processed powders and the elemental mapping of the processed powders and green samples were examined. Additionally, particle size analysis was performed on selected samples of the processed alloys by Zetasizer.

2.3. Compaction behavior of the developed [(Fe–35wt%Mn)$_{100-x}$–Cu$_x$] alloys

Compaction experiments were conducted to study the effect of the processing variables (shown in Table 1) on the densification. The compaction experiment was performed using an MTS universal

Table 1. Design input parameters (MT, MS, BPMR, and CC) and experimental results (RD, crystallite size, and lattice strain) obtained in the present study

Exp. no.	Alloy code	MT, h	BPMR, n	MS, rev/min	CC, wt%	RD, %	Crystallite size (from Fe peak), nm	Lattice strain (from Fe peak), %
1	BD0-1	5.5	10	100	0	71.65	37.0	0.3120
2	BD0-2	5.5	10	300	0	65.94	28.0	0.3340
3	BD0-3	1.0	10	200	0	66.63	32.0	0.3030
4	BD0-4	10.0	10	200	0	67.76	25.0	0.3730
5	BD0-5	5.5	5	200	0	67.99	44.0	0.2850
6	BD0-6	5.5	15	200	0	68.53	25.0	0.3760
7	BD5-1	1.0	5	200	5	75.04	58.0	0.1650
8	BD5-2	10.0	5	200	5	72.66	18.0	0.5070
9	BD5-3	1.0	15	200	5	73.49	38.0	0.2480
10	BD5-4	10.0	15	200	5	66.04	22.0	0.4180
11	BD5-5	5.5	5	100	5	75.46	58.0	0.1650
12	BD5-6	5.5	15	100	5	72.08	28.0	0.3340
13	BD5-7	5.5	5	300	5	71.20	41.0	0.2740
14	BD5-8	5.5	15	300	5	64.30	26.0	0.3550
15	BD5-9	1.0	10	100	5	75.19	58.0	0.1670
16	BD5-10	10.0	10	100	5	71.79	17.0	0.5560
17	BD5-11	1.0	10	300	5	70.98	21.0	0.4610
18	BD5-12	10.0	10	300	5	66.16	18.0	0.5050
19	BD5-13	5.5	10	200	5	69.66	22.0	0.4180
20	BD10-1	5.5	10	100	10	75.23	25.0	0.3740
21	BD10-2	5.5	10	300	10	67.80	23.0	0.4080
22	BD10-3	1.0	10	200	10	75.08	33.0	0.3360
23	BD10-4	10.0	10	200	10	67.32	28.0	0.3340
24	BD10-5	5.5	5	200	10	75.38	23.0	0.4080
25	BD10-6	5.5	15	200	10	72.19	24.0	0.4580
26	BD5-13R	5.5	10	200	5	68.99	22.0	0.4180
27	BD5-13R	5.5	10	200	5	69.12	22.0	0.4180

BPMR, ball-to-powder mass ratio; CC, Cu content; Exp. No., Experiment Number; MT, milling time; MS, milling speed; RD, relative density.

testing machine (MTS Systems Corporation, USA) and a hardened H13 tool steel die with an inner diameter of 15 mm. All compaction experiments were performed at room temperature by applying CP ranging from 25 MPa to 1,100 MPa at a loading rate of 1 mm/min. RD–CP curves were generated from the compaction experiment.

2.4. Statistical analysis

RSM, which is a tool for the design of experiments, was used to analyze the effect of the input parameters on the compressibility/densification, in terms of RD response of the studied green samples, by identifying the most significant variables affecting the densification response. The central composite design was used to perform the experimentations. Twenty-seven experiments were carried out

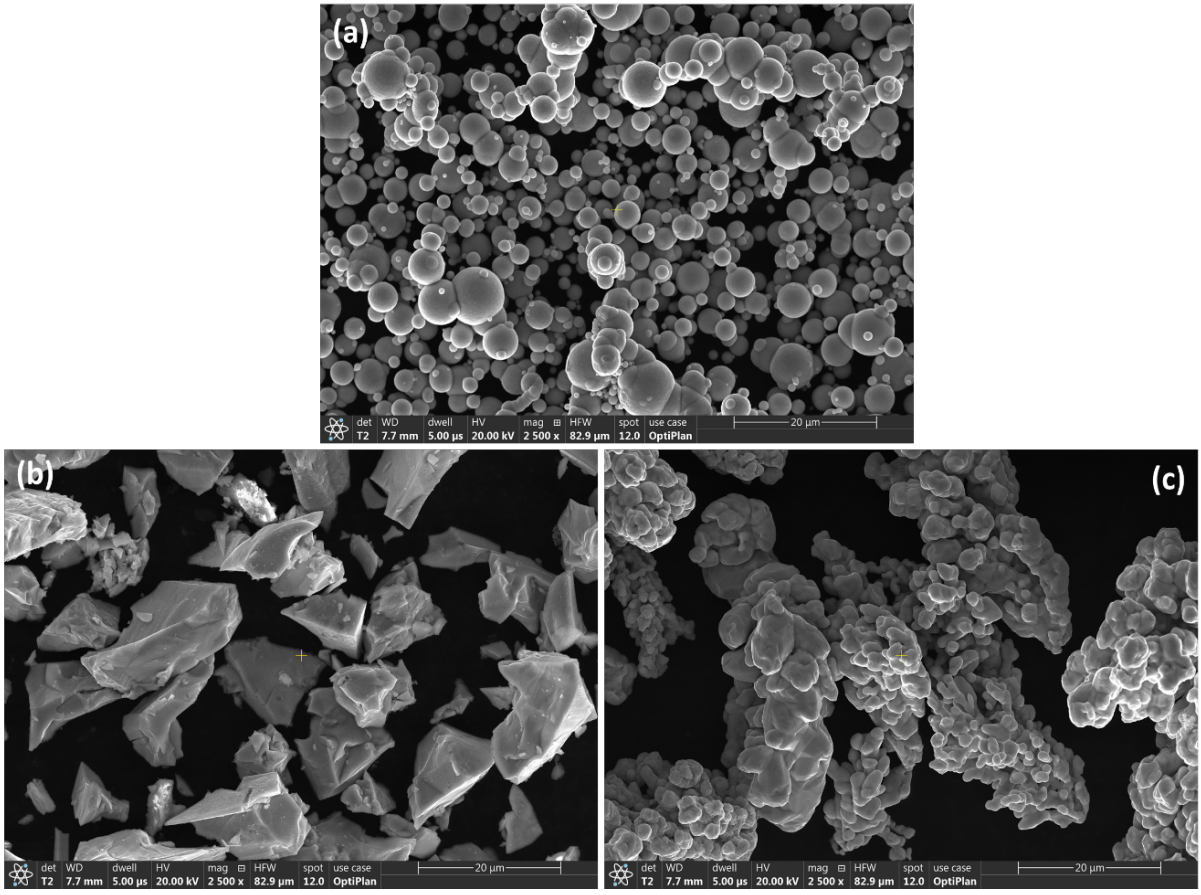


Fig. 1. SEIs of the as-received **(A)** Fe, **(B)** Mn, and **(C)** Cu powders used in the present study. SEI, secondary electron image

as given in Table 1. The repeated conditions in Table 1 (Experiments 19, 26, and 27) are essential for the design of the experiment by the central composite design. These repeated experiments are necessary for the accurate determination of the center of the space in the central composite design. The input parameters in the present study include MT, BPMR, MS, and alloy composition (CC). The measured response in this study was the RD. It should be highlighted that the RD listed in Table 1 was obtained at the maximum applied load (1,100 MPa) during compaction. The design of the experiments and the analysis of the results obtained in the present study were performed using Minitab software (version 15). ANOVA test was used to determine the most significant input parameters.

3. Results and discussion

3.1. Microstructure of the processed [(Fe–35wt%Mn)$_{100-x}$–Cu$_x$] alloy powders

Figure 1 shows the secondary electron images (SEIs) of the as-received Fe, Mn, and Cu powders used in the present study. Figure 1A illustrates the spherical particles of Fe powders with size $<$10 μm. Figure 1B displays Mn powders with facet shape and particle size $<$80 μm. Figure 1C illustrates the Cu powders' dendritic shape with an average size $<$120 μm.

Figure 2 shows the SEIs of three selected samples to illustrate the effect of BPMR and MT, as examples, on the size and morphology of the processed alloy powders. Figure 2A displays the BD5-1 alloy with processing conditions of 5 wt%Cu, 1 h MT, 200 rev/min MS, and 5:1 BPMR. Fig-

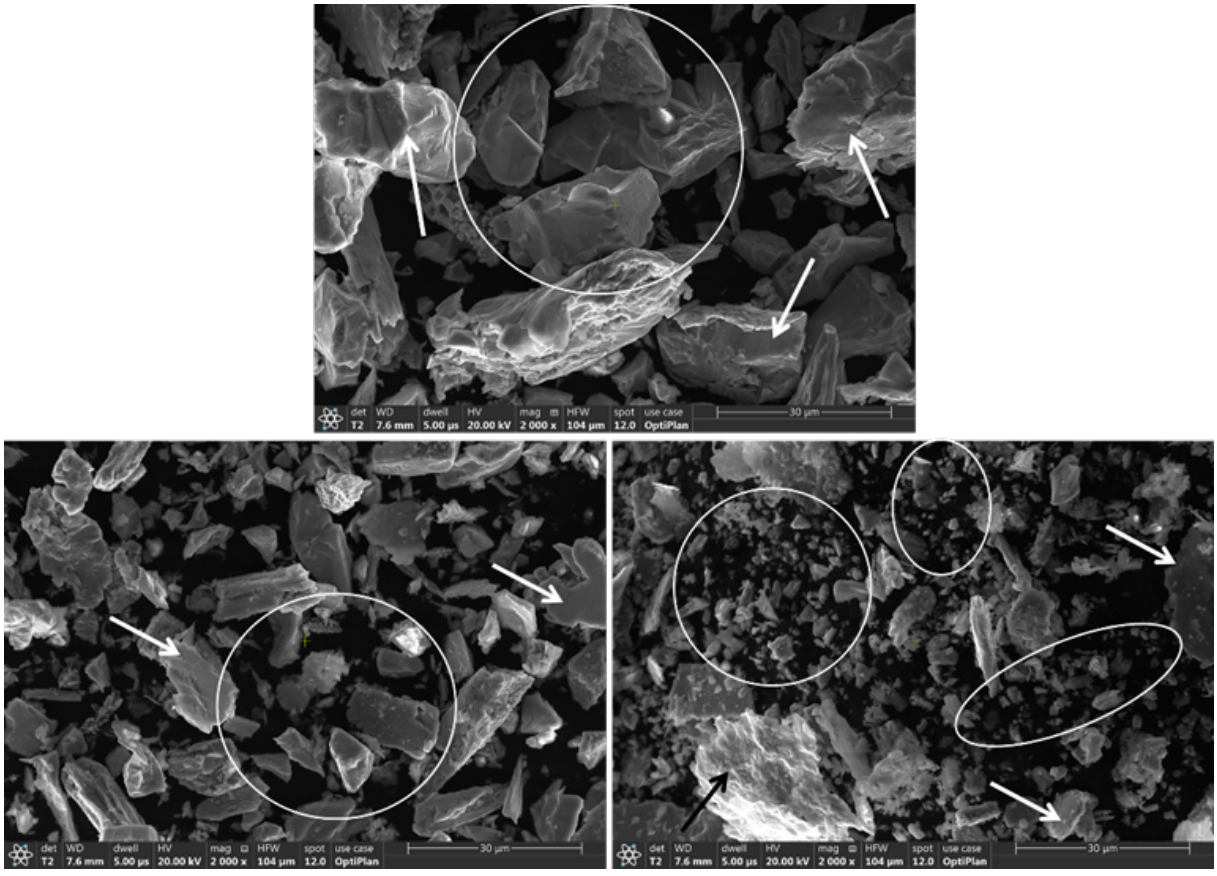


Fig. 2. SEIs of the size and shape of the selected processed alloy powders: **(A)** BD5-1; **(B)** BD5-3; and **(C)** BD5-4 alloys. SEI, secondary electron image

ure 2B exhibits the processed powders of BD5-3 alloy with input parameters of 5 wt% Cu, 1 h MT, 200 rev/min MS, and 15:1 BPMR. Figure 2C reveals the processed powders of BD5-4 alloy with conditions of 5 wt% Cu, 10 h MT, 200 rev/min MS, and 15:1 BPMR. It is obvious from these images that on increasing the BPMR (BD5-1 *vs*. BD5-3 samples), the powder particles in Figure 2B became more refined (the circled regions) and flattened (arrowed), compared with the particles in Figure 2A. Furthermore, increasing the MT (BD5-3 *vs*. BD5-4 samples), the powder particles in Figure 2C displayed a large decrease in the particle size, as seen in the circled regions, and an additional flattening in the particles' shape, as seen in the arrowed particles. Increasing MT and/or BPMR resulted in more energy input during the milling process, which applied more collision action inside the milling vails and produced finer powders, as shown in Figure 2C.

Figure 3 presents the results of the EDS analysis of the same selected alloys (BD5-1, BD5-3, and BD5-4). Figures 3A, 3D, and 3G show the SEIs for the BD5-1, BD5-3, and BD5-4 alloys, respectively. Figures 3B, 3E, and 3H show the elemental maps for the BD5-1, BD5-3, and BD5-4 alloys, respectively; these maps are in full agreement with the results shown in Figure 2. The EDS spectra in Figures 3C, 3F, and 3I confirm the alloys' chemical composition. Increasing BPMR from 5:1 in the BD5-1 alloy – shown in Figures 3A and 3B – to 15:1 in the BD5-3 alloy – shown in Figures 3D and 3E – was observed to improve the elemental dispersion, with a notable refining in the metal particles. Moreover, increasing the MT from 1 h in BD5-3 alloy (illustrated in Figures 3D and 3E) to

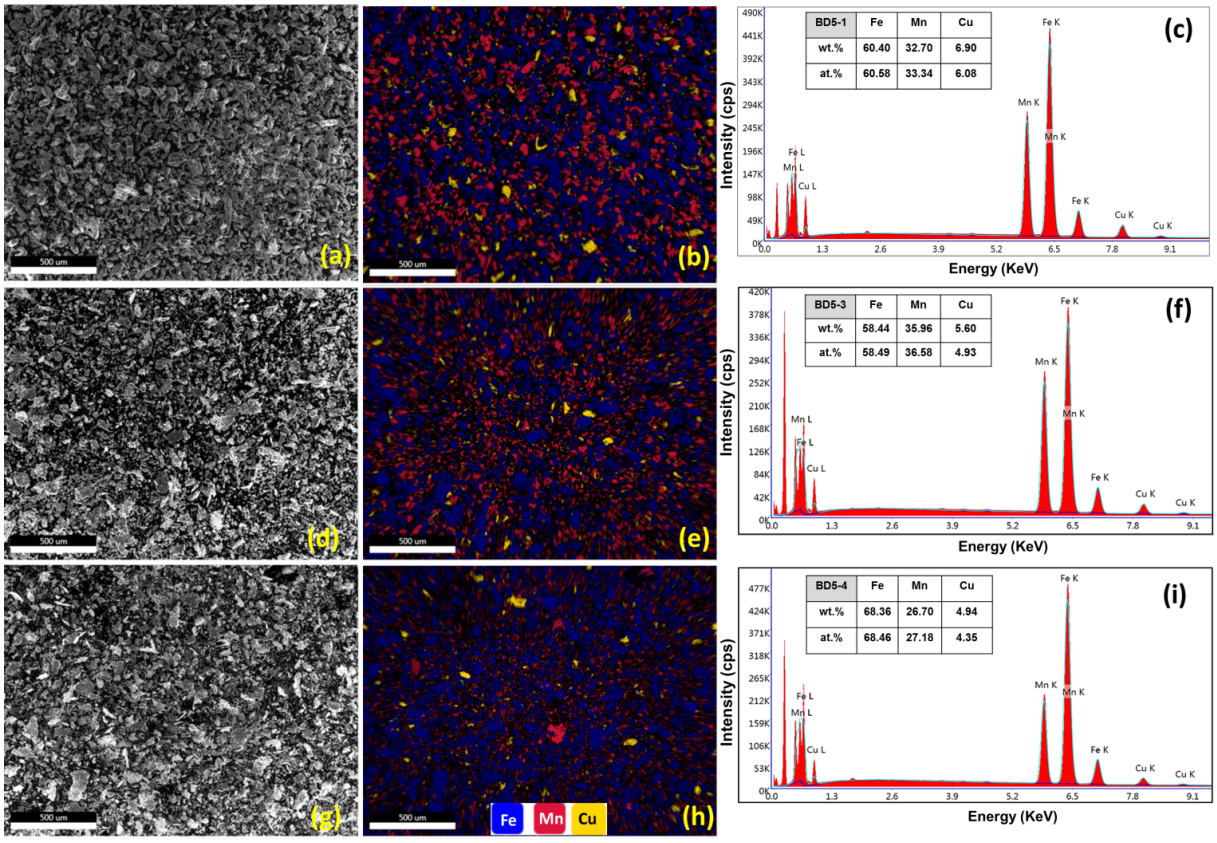


Fig. 3. Results of EDS analysis of the alloys in powder form: **(A–C)** BD5-1; **(D–F)** BD5-3; **(G–I)** BD5-4. EDS, energy dispersive spectroscopy

10 h in BD5-4 alloy (shown in Figures 3G and 3H) resulted in an additional refining of the powder particles and improved the elemental dispersion with a notable flattening/deformation of Fe particles due to milling action.

3.2. Analysis of the particle size of the processed [(Fe–35 wt%Mn)$_{100-x}$–Cu$_x$] alloys

The alloys selected for particle size analysis include the following: BD5-1 *vs.* BD5-2 and BD5-9 *vs.* BD5-10 to show the effect of MT; BD5-2 *vs.* BD5-4 to illustrate the impact of BPMR; and BD5-9 *vs.* BD5-11 to display the influence of MS, as shown in Table 1. Figure 4 and Table 2 display the results of particle size analysis of the selected samples. The average particle size of the selected samples was measured based on the main peak shown in Figure 4. Figure 4 and Table 2 show that increasing the MT from 1 h (BD5-1 sample) to 10 h (BD5-2 sample) resulted in decrease in the average particle size from 1,477 nm to 655.40 nm, respectively. Moreover, raising the

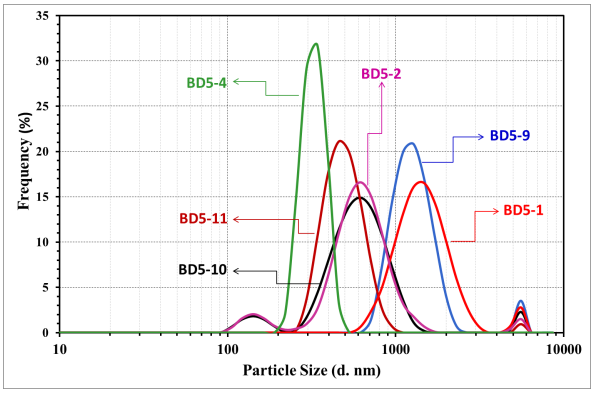


Fig. 4. The distribution of particle size for BD5-1, BD5-2, BD5-4, BD5-9, BD5-10, and BD5-11 alloys. d, diameter

Table 2. The results of particle size analysis for selected alloys

Alloy code	Average particle size, nm	Standard deviation, nm	% intensity (main peak)	PDI
BD5-1	1,477.00	480.50	96.50	0.33
BD5-2	655.40	220.30	91.20	0.49
BD5-4	327.10	53.28	100.00	0.52
BD5-9	1,274.00	315.90	96.20	0.42
BD5-10	638.70	214.10	91.10	0.41
BD5-11	499.50	129.40	99.10	0.35

PDI, polydispersity index.

BPMR from 5:1 (BD5-2 alloy) to 15:1 (BD5-4 alloy) resulted in an additional decrease in the average particle size from 655.40 nm to 327.10 nm, respectively. Furthermore, increasing the MT from 1 h (BD5-9 sample) to 10 h (BD5-10 sample) resulted in decrease in the average particle size from 1,274 nm to 638.70 nm, respectively. In addition, raising the MS from 100 rev/min (BD5-9 alloy) to 300 rev/min (BD5-11 alloy) resulted in a significant decrease in the average particle size from 1,274 nm to 499.50 nm, respectively. The results presented in Figure 4 and Table 2 confirmed the effect of ball milling input parameters (MT, BPMR, and MS) on the particle size of the processed powders. Increasing one or more of the input parameters resulted in a significant effect in terms of decreasing the particle size of the processed powders due to the increased energy input of milling and the strong mutual collision among powders, balls, and vail walls. These effects activate the common mechanism of mechanical alloying, which includes deformation, welding, breaking, and rewelding of the particles, leading to increased particle refining and alloying of the mixed powders. The polydispersity index (PDI) values listed in Table 2 confirmed the uniformity of the obtained particle size for the processed alloys, and the distribution of these particle sizes lies over a narrow range. Generally, a PDI value <0.7 indicates an even distribution of particle size over a small size range, which is the case for all samples presented in Table 2 and Figure 4.

3.3. XRD results analysis of the processed [(Fe–35 wt%Mn)$_{100-x}$–Cu$_x$] alloys

XRD analysis was performed on all samples to illustrate the effect of the input parameters of ball milling on the crystallite size and homogeneous lattice strain of the processed powders. The results of the selected samples (from Table 1) are discussed in this section. The selected samples include BD5-1 *vs*. BD5-2 to display the effect of MT; BD5-1 *vs*. BD5-3 to reveal the influence of BPMR; and BD5-9 *vs*. BD5-11 alloys to show the effect of MS. Figure 5 displays the XRD patterns of all samples for XRD analysis. The peaks were identified using X'Pert High Score Plus software, where the Fe [reference International Centre for Diffraction Data [ICDD]: 01-089-4186, space group: Im-3m(229)], Mn [reference ICDD: 00-001-1237, space group: I-43m(217)], and Cu [reference ICDD: 01-085-1326, space group: Fm-3m(225)] peaks were recognized, as illustrated in Figure 5. The estimated lattice strain and crystallite size are listed in Table 1. These features were determined using X'Pert High Score Plus software based on the major Fe peak only in each XRD pattern. With regard to the crystallite size, it was observed that increasing the MT from 1 h to 10 h resulted in a notable decrease in the crystallite size at various BPMRs and different MSs. The determined crystallite size for the BD5-1 sample milled for 1 h was 57.7 nm, compared with 18.2 nm in the case of the BD5-2 sample milled for 10 h. Similar observations when increasing the MT from 1 h to 10 h but at large BPMRs (BD5-3 *vs*. BD5-4 alloys) led to decrease in the crystallite size from 37.7 nm to 22.3 nm, respec-

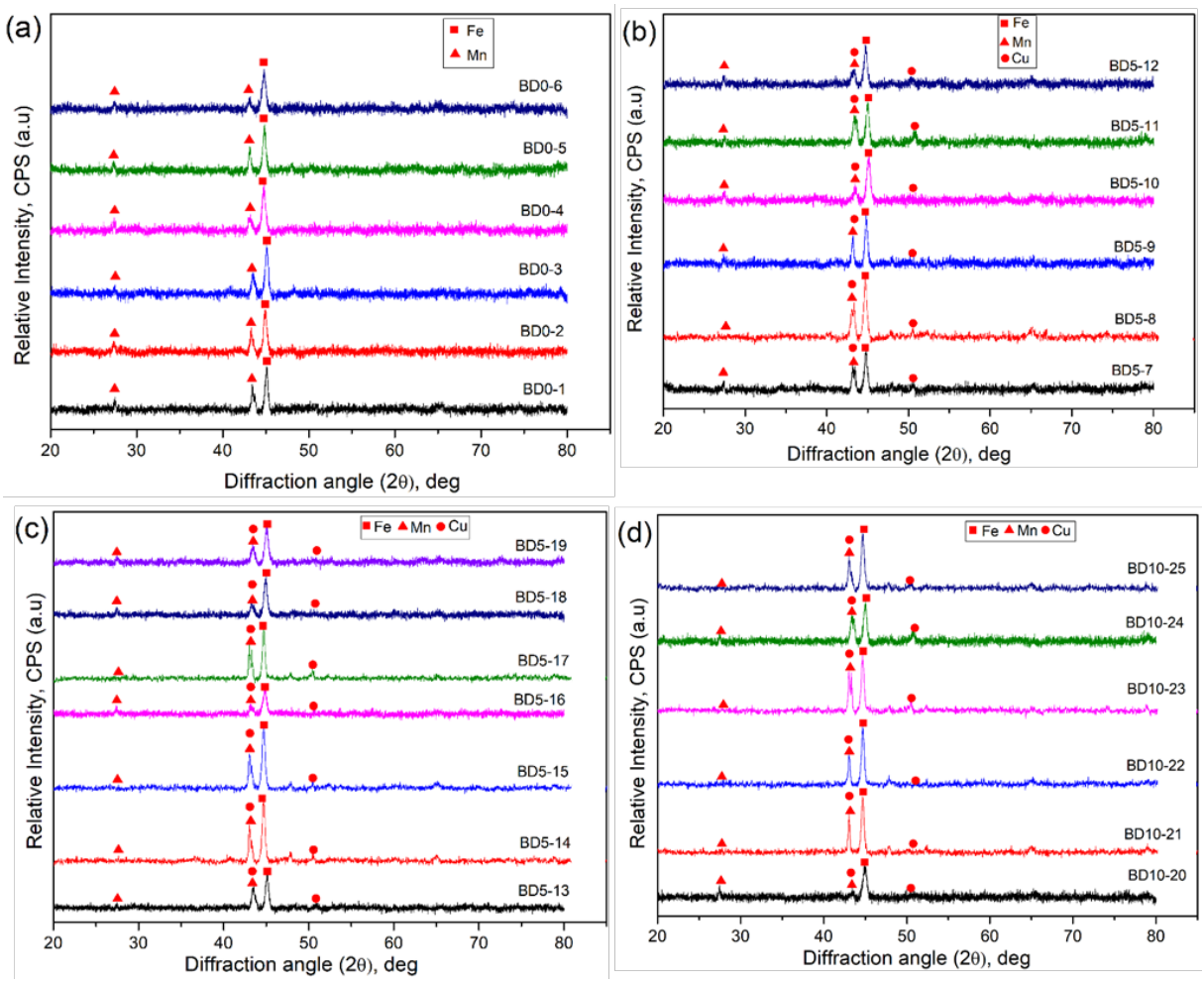


Fig. 5. XRD patterns of all powder samples: **(A)** BD0-1 to BD0-6; **(B)** BD5-7 to BD5-12; **(C)** BD5-13 to BD5-19; **(D)** BD10-20 to BD10-25. CPS, counts/s; XRD, X-ray diffraction

tively. The homogeneous lattice strain was noted to increase with increase in the MT, as shown in Table 1. For example, the estimated lattice strain for the BD5-1 alloy milled for 1 h was 0.165%, compared with 0.507% in the case of the BD5-2 alloy milled for 10 h. The effect of BPMR on the crystallite size and lattice strain was also examined, as listed in Table 1. For instance, increasing the BPMR from 5:1 (BD5-1 alloy) to 15:1 (BD5-3 alloy) led to a reduction in the crystallite size from 57.7 nm to 37.7 nm and an increase in the homogeneous lattice strain from 0.165% to 0.248%. Furthermore, the effect of MS on the crystallite size and lattice strain was investigated, as listed in Table 1. The increase in MS from 100 rev/min (BD5-9 alloy) to 300 rev/min (BD5-11 alloy) led to a considerable decrease in crystallite size from 57.6 nm to 21.3 nm and a substantial increase in the homogeneous lattice strain from 0.167% to 0.461%. Furthermore, increasing the energy input of the milling process resulted in elemental dispersion and alloying through the common mechanism of mechanical alloying, including deformation, welding, breaking, and rewelding of the elemental powders, leading to increased elemental alloying/dissolution of the mixed powders. For example, when comparing BD5-9 *vs*. BD5-11 samples, the energy input of milling for the BD5-11 alloy is higher than that of the BD5-9 alloy due to the high MS of 300 rev/min. Consequently, BD5-11 alloy displays greater peak

broadening in the XRD patterns, with the disappearance of some peaks, compared with the XRD pattern of the BD5-9 alloy in Figure 5. These observations match the elemental mapping analysis presented in the next section wherein increased elemental dispersion and low agglomeration were observed for BD5-11 compared with the BD5-9 sample. These are indications of the formation of large extents of solid solution in the BD5-11 alloy compared with the BD5-9 alloy. Therefore, the extent of solid solution formation in the processed samples depends on the input parameters of the process. These findings ascertain that these parameters (MT, BPMR, and MS) play a major role in determining the microstructure features of the processed alloys. Augmenting the MT and/or BPMR and/or MS produced a substantial effect in terms of decreasing the crystallite size, increasing the lattice strain, and increasing the extent of solid solution formation. All these changes directly affect the subsequent material behavior, such as the compressibility and densification of the powders, as elaborated in the following sections.

3.4. Densification analysis of the processed [(Fe–35 wt%Mn)$_{100-x}$–Cu$_x$] alloys

The compaction experiments were performed according to the input parameters listed in Table 1. The RDs at the maximum pressure applied at 1,100 MPa are shown in Table 1. Figure 6 displays the RD versus compaction load for selected samples of [(Fe–35 wt%Mn)$_{95}$–Cu$_5$]. From Figure 6, it is obvious that the RD for all samples revealed a continuous improvement with increase in the CP. However, the improvement rate in RD varied according to the controlling mechanisms of powder compressibility [32]. From Figure 6, a sharp increase in the RD of the samples up to ∼ 60 MPa is seen due to the particle ordering and rapid reduction in the spacing among the powders. Figure 6 also shows that in the CP ranging from ∼ 60 MPa to ∼ 200 MPa, the RD is still increasing but with a reduced slope due to the predominant mechanism of powder deformation, which led to extra contact areas among the powders and reduced pores [34]. Pressures >200 MPa were observed to produce more improvements in the compressibility until the maximum values of RD were reached at 1,100 MPa; however, the curve in this region revealed a lower slope due to the increased strain hardening of the powders, which resist further deformation and impede additional increase in the contact areas among powders [35]. With regard to the behavior of the selected samples presented in Figure 6, these 13 samples displayed the same general behavior of RD versus CP; however, these samples did not reveal the same RD at the applied loads, specifically, at the maximum CP of 1,100 MPa. The BD5-5 alloy displayed the maximum RD (75.46%), while the BD5-8 alloy exhibited the minimum RD (64.30%). The remaining 11 samples presented in Figure 6 were observed to display various RD values with CP between the maximum and minimum behaviors according to the various input parameters (Table 1). The sample with exceedingly high energy of ball milling involving the highest BPMR (15:1) and MS (300 rev/min) displayed the least value of RD due to the large stored energy, increased lattice strain, and great amount of work hardening in the processed powders. Therefore, the processed powders resist the compaction process and the final RD was reduced. On the other hand, the highest RD in Figure 6 was attained with a moderate energy of ball milling, which included BPMR (5:1), and MS (100 rev/min); in this case, the processed powders

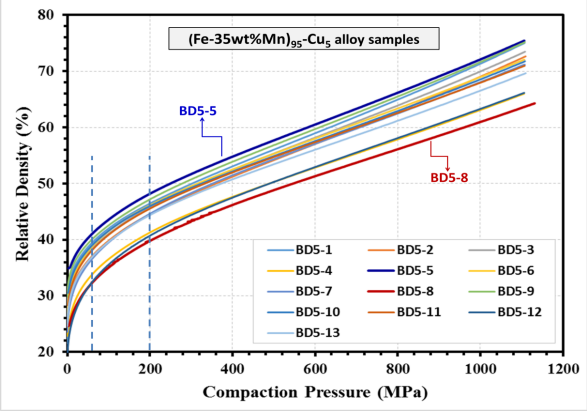


Fig. 6. The experimental results of RD versus CP for [(Fe–35 wt%Mn)$_{95}$–Cu$_5$] green samples. CP, compaction pressure; RD, relative density

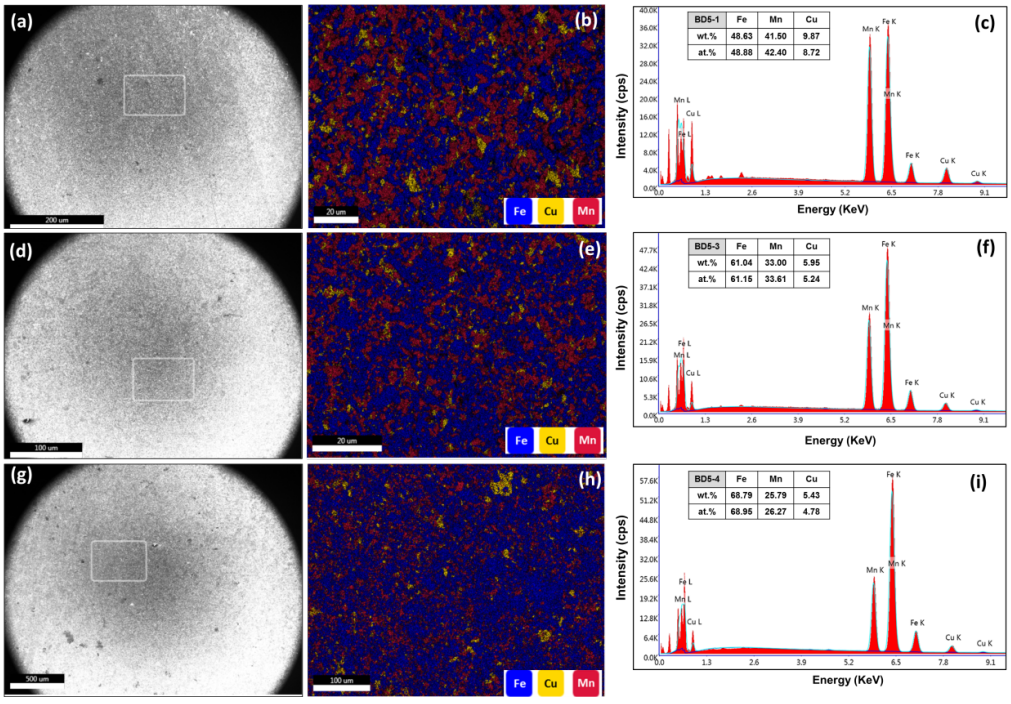


Fig. 7. EDS analysis results of the compacted samples: **(A–C)** BD5-1; **(D–F)** BD5-3; and **(G–I)** BD5-4. EDS, energy dispersive spectroscopy

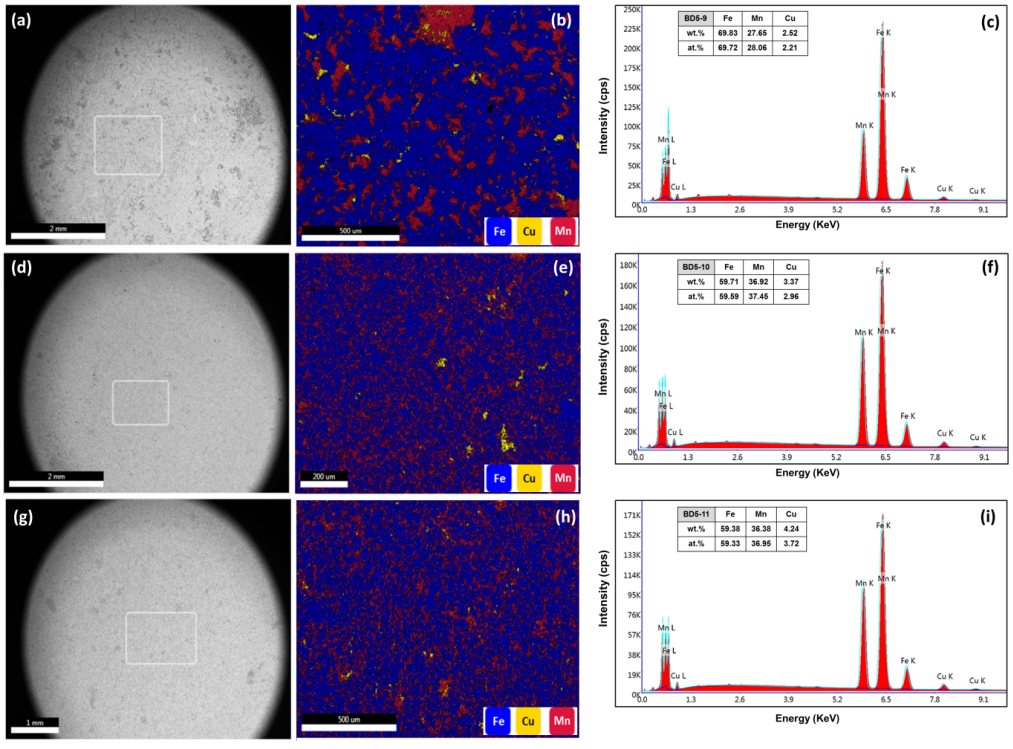


Fig. 8. EDS analysis results of the green samples: **(A–C)** BD5-9; **(D–F)** BD5-10; and **(G–I)** BD5-11. EDS, energy dispersive spectroscopy

were still deformable with minimum strain hardening effect, which permitted more compressibility and enhanced the RD of the powders.

Figures 7 and 8 show the effect of the input parameters (MT, BPMR, and MS) on the microstructure of these compacted green samples on investigation of the selected green samples by EDS analysis. Figures 7, 8A, 8D, and 8G reveal the SEI of the green compacts collected from the selected samples. The chemical composition of the selected samples was confirmed by the EDS spectra in Figures 7, 8C, 8F, and 8I. Figures 7, 8B, 8E, and 8H show the elemental mapping accomplished on the outlined regions of the selected samples. From the maps presented in Figures 7B, 7E, and 7F, it can be observed that increasing the BPMR from 5:1 (BD5-1 alloy) to 15:1 in (BD5-3 alloy) resulted in improvement in the elemental dispersion with a notable refining in the microstructure constituents, as shown in Figures 7B and 7E, respectively. Additionally, increasing the MT from 1 h (BD5-3 alloy) to 10 h (BD5-4 alloy) resulted in an additional refining of the microstructure constituents and enhanced dispersion of the elements, as revealed in Figures 7E and 7H, respectively. From the maps presented in Figures 8B, 8E, and 8F, it can be noticed that a similar effect was observed when increasing the MT from 1 h (BD5-9 alloy) to 10 h (BD5-10 alloy). Increasing the MS from 100 rev/min (BD5-9 alloy) to 300 rev/min (BD5-11 alloy) resulted in an extra refining of the microstructure constituents and an additional enhancement in the dispersion of the elements, as revealed in Figures 8E and 8H, respectively.

EDS analysis was used in the present study for qualitative and quantitative analyses of the microstructure of the powders and green samples obtained under different processing conditions. With regard to the accuracy of the quantitative EDS analysis, it depends on the structural homogeneity and density of the examined alloys. In general, quantitative EDS analysis of standard dense alloys with a homogeneous structure provides high accuracy and low scattering. On the other hand, a scattering in EDS results is attained for experimental samples that reveal low density and a relatively segregated microstructure. In the present study, the examined samples were in powder and green forms and were subjected to different processing variables (MT, MS, and BPMR), as shown in Table 1. Accordingly, these examined samples displayed different homogeneity levels and densities. In this case, qualitative analysis was used to perfectly illustrate elemental dispersion and other features such as microstructure refinement. Chemical analysis of the examined samples confirmed the presence of the alloying elements and their dispersion profiles for each sample; however, there was scattering in the quantitative chemical analysis values, which could be attributed to variations in the processing variables, the differences in sample homogeneity levels, and the low densities for the examined samples. The same reasons are responsible for the considerable influence observed on the compaction behavior of the samples, as shown in Figure 6 and the RD values listed in Table 1.

3.5. ANOVA results for all the responses

With regard to the input parameters and the experimental results displayed in Table 1, the ANOVA test was performed to identify the input parameters having significant and nonsignificant influence on the crystallite size, lattice strain, and compactibility/densification of the processed alloys in terms of RD. The results of the ANOVA test for all responses are shown in Tables 3–5 for the crystallite size, lattice strain, and RD, respectively. Tables 3–5 list the estimated statistical terms such as sum of squares, degree of freedom (DF), mean square, F-value, and p-value. The p-value is used to decide the significance of the input parameters [39]. According to the ANOVA test, a p-value < 0.0500 indicates the significance of the model terms, while p-value > 0.1000 refers to model terms that are nonsignificant [40]. Based on the ANOVA results for the crystallite size (Table 3), the most significant influencing linear parameter is the MT, followed by BPMR and MS. The Cu content was found to be a nonsignificant parameter. The square term of MT $\times$ MS also slightly influenced the crystallite size. Similarly, based on the ANOVA results for the lattice strain (Table 4), the only significant parameter was the lattice strain,

Table 3. The results of the ANOVA test performed for the crystallite size

Source	Sum of squares	DF	Mean square	*F*-value	*p*-value
Model	2.696 × 105	10	26,963.56	3.89	0.0079
MT	1.025 × 105	1	1.025 × 105	14.78	0.0014
BPMR	56,033.33	1	56,033.33	8.08	0.0118
MS	33,920.33	1	33,920.33	4.89	0.0419
CC	12,610.08	1	12,610.08	1.82	0.1963
(MT) × (BPMR)	14,520.25	1	14,520.25	2.09	0.1672
(MT) × (MS)	36,100.00	1	36,100.00	5.20	0.0366
(MT) × (CC)	144.00	1	144.00	0.0208	0.8872
(BPMR) × (MS)	5,402.25	1	5,402.25	0.7789	0.3906
(BPMR) × (CC)	7,225.00	1	7,225.00	1.04	0.3226
(MS) × (CC)	1,190.25	1	1,190.25	0.1716	0.6842
Residual	1.110E × 105	16	6,936.07		
Lack of Fit	1.109E × 105	14	7,923.37	316.93	0.0031
Pure Error	50.00	2	25.00		
Total	3.806 × 105	26			

ANOVA, analysis of variance; BPMR, ball-to-powder mass ratio; CC, Cu content; DF, degree of freedom; MS, milling speed; MT, milling time.

Table 4. The results of the ANOVA test performed for the lattice strain

Source	Sum of squares	DF	Mean square	*F*-value	*p*-value
Model	0.1630	10	0.0163	2.49	0.0499
MT	0.0855	1	0.0855	13.08	0.0023
BPMR	0.0128	1	0.0128	1.96	0.1807
MS	0.0147	1	0.0147	2.25	0.1532
CC	0.0092	1	0.0092	1.41	0.2518
(MT) × (BPMR)	0.0074	1	0.0074	1.13	0.3032
(MT) × (MS)	0.0298	1	0.0298	4.55	0.0487
(MT) × (CC)	0.0013	1	0.0013	0.1983	0.6621
(BPMR) × (MS)	0.0019	1	0.0019	0.2962	0.5938
(BPMR) × (CC)	0.0003	1	0.0003	0.0442	0.8361
(MS) × (CC)	0.0001	1	0.0001	0.0169	0.8983
Residual	0.1046	16	0.0065		
Lack of fit	0.1045	14	0.0075	355.54	0.0028
Pure error	0.0000	2	0.0000		
Total	0.2676	26			

ANOVA, analysis of variance; BPMR, ball-to-powder mass ratio; CC, Cu content; DF, degree of freedom; MS, milling speed; MT, milling time.

and all other input parameters were not much significant. The results of the ANOVA test presented in Table 5 illustrate that all linear terms such as MT, BPMR, MS, and CC are statistically significant. Furthermore, only one interaction term (MT × CC) was observed to display statistical significance.

Table 5. The results of ANOVA test performed for the RD

Source	Sum of squares	DF	Mean square	*F*-value	*p*-value
Model	274.0800	10	27.4100	12.2300	<0.0001
MT	50.7600	1	50.7600	22.6400	0.0002
BPMR	37.1000	1	37.1000	16.5500	0.0009
MS	102.2000	1	102.2000	45.5900	<0.0001
CC	50.0200	1	50.0200	22.3100	0.0002
(MT) × (BPMR)	6.4300	1	6.4300	2.8700	0.1098
(MT) × (MS)	0.5041	1	0.5041	0.2249	0.6418
(MT) × (CC)	19.7600	1	19.7600	8.8100	0.0090
(BPMR) × (MS)	3.1000	1	3.1000	1.3800	0.2570
(BPMR) × (CC)	3.4800	1	3.4800	1.5500	0.2308
(MS) × (CC)	0.7396	1	0.7396	0.3299	0.5737
Residual	35.8700	16	2.2400		
Lack of fit	35.6100	14	2.5400	20.1700	0.0482
Pure error	0.2522	2	0.1261		
Total	309.9500	26			

ANOVA, analysis of variance; BPMR, ball-to-powder mass ratio; CC, Cu content; DF, degree of freedom; MS, milling speed; MT, milling time; RD, relative density.

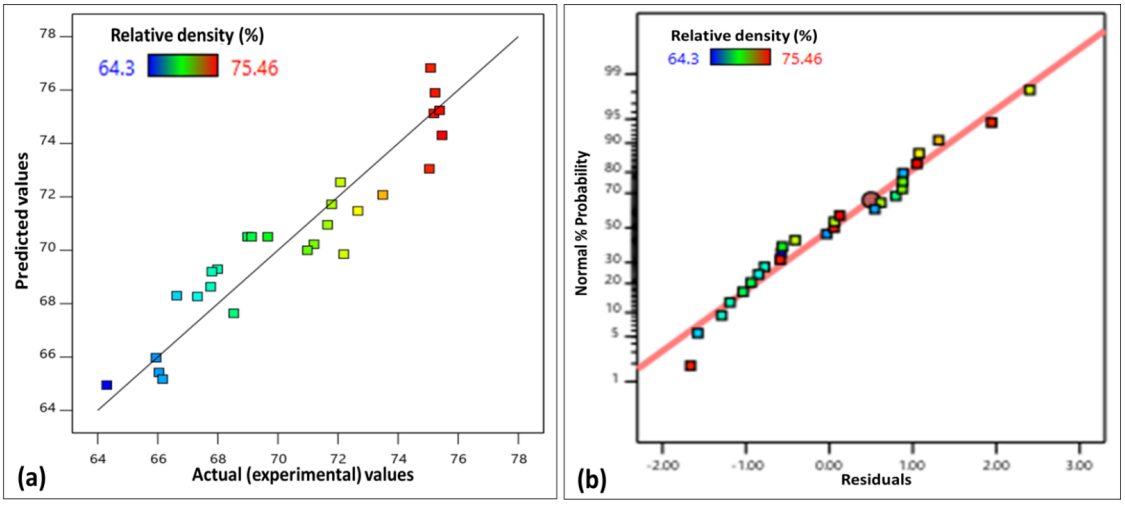


Fig. 9. ANOVA results of RD: **(A)** The experimental and the predicted values of RD; and **(B)** normal probability of residuals of RD of the developed compacted samples. RD, relative density

As an example, the correlation of the experimental and predicted results for RD with the corresponding normal probability of residuals is presented in Figure 9. Figure 9A reveals the actual RD experimental values versus the predicted values by the statistical analysis performed in the present study. Figure 9B displays the normal %probability versus residual, which assesses the model validity. Figures 9A and 9B show that almost all data points are adjacent to the straight line, which confirms the accuracy of the statistical analysis results obtained in the present study and the robust relationship between the predicted RD and the experimental results.

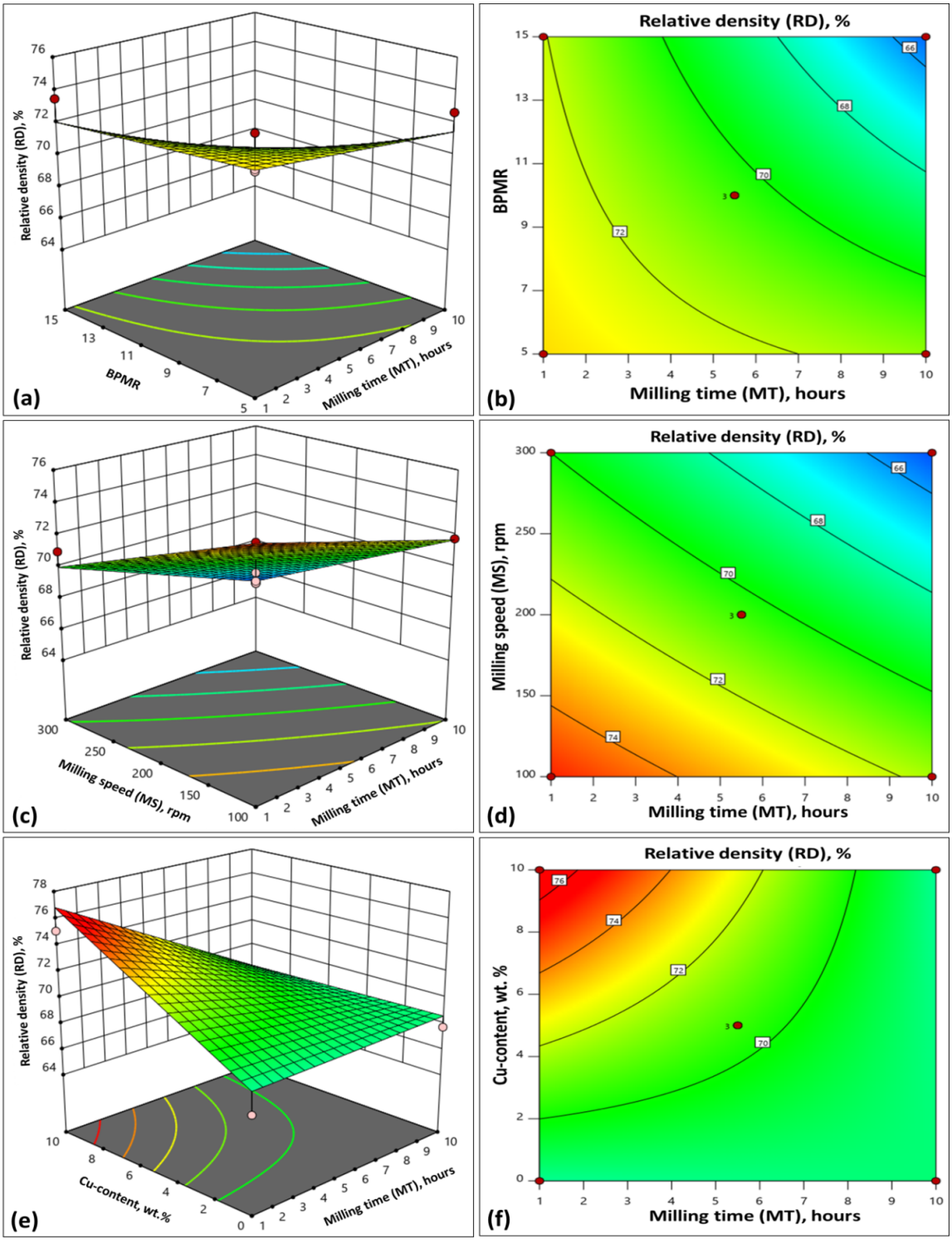


Fig. 10. The impact of the input variables on the RD of the developed green samples: **(A, C, E, G, I, K)** 3D surface plots; **(B, D, F, H, J, L)** 2D contour plots. RD, relative density

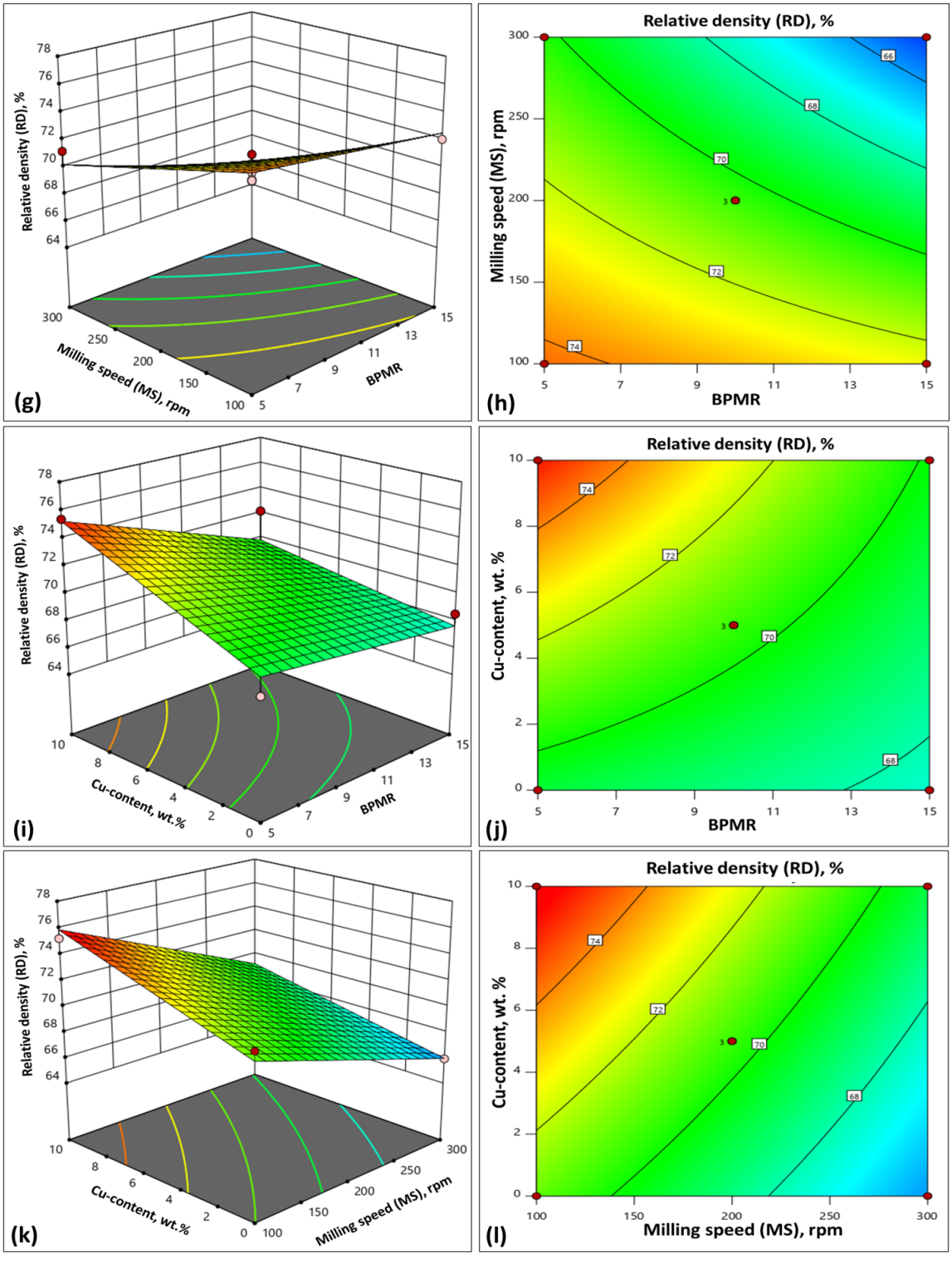


Fig. 10. ...continued

3.6. The effect of variables on the compactibility/RD of the developed [(Fe–35wt%Mn)$_{100-x}$–Cu$_x$] alloys

The impact of the input variables on the compactibility/RD of the developed alloy systems is presented in the form of 3D surface plots and 2D contour plots, as shown in Figure 10. Figure 10 (A–L) can be used for forecasting the RDs of the studied alloys. Figures 10A and 10B reveal the effect of the MT and BPMR on the RD. From the surface plot in Figure 10A and the contour plot in Figure 10B, it can be observed that the optimum RD and compressibility can be attained by decreasing the MT and BPMR. This behavior is due to the fact that increasing the MT and the BPMR results in increasing the energy of milling, which leads to increased lattice strain (as discussed in Section 3.3) and excessive plastic deformation of the powders [32]. The increased lattice strain and severe deformation of the powders impede the compressibility of the powders and decrease the RD [35]. Figures 10C and 10D show the impact of the MT and MS on the RD. From Figures 10C and 10D, it can be noticed that the RD decreased on increasing the MT and MS. Increasing the MT and speed led to high energy input during milling, which produced extra work-hardened powders with a substantial amount of lattice strain, which resists the compression and reduces the RD [34]. Figures 10E and 10F reveal the impact of MT and CC on the RD. Concerning Figures 10E and 10F, it can be seen that the RD improved by decreasing the MT and increasing the CC. Increasing the CC led to an improved RD because copper is a ductile element and increasing its content promoted the mechanism of compaction process through providing more deformability of the powders. Figures 10G and 10H illustrate the influence of MS and BPMR on the RD; it can be observed that the powder's compactibility and RD were enhanced on reducing the MS and/or BPMR due to the decreased power input during milling. Figures 10I and 10J show the influence of BPMR and CC on the RD, and it can be concluded that the powder's compactibility and RD were enhanced on increasing the CC and/or reducing the BPMR. Figures 10K and 10L display the influence of MS and CC on the RD; it can be perceived that the RD was enhanced on reducing the MS and/or increasing the CC.

The abovementioned sections covered the investigation into the effect of the input parameters on the microstructure and compactibility/RD of the developed alloys. Based on this analysis, selecting the input parameters to attain the desired microstructure features and improved densification behavior is a challenge. It was found that increasing the ball milling parameters (MT, MS, and BPMR) resulted in significant enhancements in the microstructure, such as uniform elemental dispersion and reduced segregation of the developed alloys (e.g., Figures 7 and 8). Additionally, increases in the input parameters produced refined particles with a substantial decrease in their crystallite size (see Tables 2 and 3). On the other hand, increasing these parameters exhibited an undesirable influence on the powder compactibility and RD of the developed alloys, as displayed in Figure 10. Increasing MT, MS, and/or BPMR resulted in high amounts of stored energy, increased lattice strain, and large amount of work hardening in the processed powders. Therefore, the processed powders resist the compaction process, and the attained RD was negatively affected. Accordingly, a recommended combination of the milling parameters was selected to provide the optimum compromise among the microstructure features and powder compressibility/RD of the developed alloys. Based on the surface and contour plots shown in Figure 10, the following conditions would provide a reasonable combination of milling conditions to attain an acceptable compromise of enhanced microstructure features and improved compactibility and RD: MT – 5 h; MS – 150 rev/min; and BPMR – 10:1. In addition, as discussed earlier, increasing the CC resulted in a substantial improvement in the RD of the developed alloys; hence, 10 wt% Cu is recommended.

4. Conclusions

- (Fe–35wt%Mn)$_{100-x}$–Cu$_x$ samples were processed (where x = 0 wt%, 5 wt%,

and 10 wt%) using ball milling; a total of 27 alloy samples were produced, as green compacts, using various processing variables.

- ANOVA test results confirmed that the input parameters MT (1–10 h), BPMR (5:1–15:1), MS (100–300 rev/min), and CC (0–10 wt%) are statistically significant.
- Increasing the milling power during ball milling by raising the MT to 10 h, the MS to 300 rev/min, and/or BPMR up to 15:1 resulted in significant enhancements in the microstructure, such as uniform elemental dispersion, reduced segregation, refinement of particles, and a substantial decrease in the crystallite size to 18 nm, e.g., in the BD5-12 sample.
- Raising the energy input during ball milling, by increasing MT, MS, and/or BPMR, led to a detrimental influence on the compressibility and RD of the developed alloys, with the minimum RD of the BD5 alloys being 64.30% for the BD5-8 alloy, while the BD5-5 alloy displayed the maximum RD of 75.46%.
- Increasing the CC resulted in a substantial improvement in the compressibility and RD of the studied alloys, whereby the BD0-5 alloy with 0 wt% Cu displayed 67.99% RD, while the BD10-5 alloy with 10 wt% Cu with the same milling variables showed 75.38% RD.
- The combination of the studied variables recommended to attain an acceptable compromise of enhanced microstructure features and improved compaction behavior and RD includes the following: MT for 5.5 h, MS for 200 rev/min, BPMR of 10:1, and CC of 10 wt%.

Data Availability Statement

The experimental data sets obtained from this research work and the results arrived after analysis during the current study are available from the corresponding author on reasonable request.

Acknowledgements

The authors gratefully acknowledge Qassim University, represented by the Deanship of Scientific Research, on the financial support for this research under the number (5583-qec-2019-2-2-I) during the academic year 1440 AH/2019 AD.

Conflict of interest

The authors declare no conflict of interest.

References

[1] Suryanarayana C. Mechanical alloying and milling. Prog Mater Sci. 2001;46:1–184. https://doi.org/10.1016/S0079-6425(99)00010-9.

[2] Koch CC. Intermetallic matrix composites prepared by mechanical alloying – a review. Mater Sci Eng A. 1998;A244:39–48. https://doi.org/10.1016/S0921-5093(97)00824-1.

[3] Bhadeshia HH. Mechanically alloyed metals. J Mater Sci Technol. 2000;1:1404–11. https://doi.org/10.1179/026708300101507361.

[4] Koch CC, Whittenberger JD. Review: mechanical milling/alloying of Intermetallic. Intermetallics. 1996;4:339–55. https://doi.org/10.1016/0966-9795(96)00001-5.

[5] Shaikh MA, Iqbal M, Akhter JI, Ahmad M, Zaman Q, Akhtar M, et al. Alloying of immiscible Ge with Al by ball milling. Mater Lett. 2003;57:3681–5. https://doi.org/10.1016/S0167-577X(03)00149-6.

[6] Ma E, Atzmon M. Phase transformations induced by mechanical alloying in a binary system. Mater Chem Phys. 1995;39:249–67. https://doi.org10.1016/0254-0584(94)01446-N.

[7] Romankov S, Sha W, Kaloshkin SD, Kaevitser K. Formation of Ti-Al coatings by mechancial alloying method. Surf Coat Technol. 2006;201:3235–45. https://doi.org/10.1016/j.surfcoat.2006.06.044.

[8] Bajakke PA, Malik VR, Saxena KK, Deshpande AS. A novel ultrahigh conductive Al-Cu composite produced via microwave sintering and post- treated by friction stir process. Adv Mater Process Technol. 2021; https://doi.org/10.1080/2374068X.2021.1945270.

[9] El-Eskandarani MS. Mechanical alloying for fabrication of advanced engineering materials. New York, U.S.A: Noyes Publications, William Andrew Publishing; 2001. pp. 22–60.

[10] Gaffet E. Ball milling: an E-v-T parameter phase diagram. Mater Sci Eng A. 1991;135:291–3. https://doi.org/10.1016/0921-5093(91)90578-B.

[11] Suryanarayana C, Chen GH, Froes FS. Milling maps for phase identification during mechanical alloying. Scripta Metall Mater. 1992;26:1727–32. https://doi.org/10.1016/0956-716X(92)90542-M.

[12] Alshataif YA, Sivasankaran S, Al-Mufadi FA, Alaboodi AS, Ammar HR. Synthesis, microstructures and mechanical behaviour of $Cr_{0.21}Fe_{0.20}Al_{0.41}Cu_{0.18}$ and $Cr_{0.14}Fe_{0.13}Al_{0.26}Cu_{0.11}Si_{0.25}Zn_{0.11}$ nanocrystallite en-

tropy alloys prepared by mechanical alloying and hot-pressing. Met Mater Int. 2021;27:139–55. https://doi.org/10.1007/s12540-020-00660-6.

[13] Clinktan R, Senthil V, Ramkumar KR, Sivasankaran S, Al-Mufadi FA. Effect of boron carbide nano particles in $CuSi_4Zn_{14}$ silicone bronze nanocomposites on matrix powder surface morphology and structural evolution via mechanical alloying. Ceram Int. 2019;45:3492–501. https://doi.org/10.1016/j.ceramint.2018.11.007.

[14] Hermawan H. Updates on the research and development of absorbable metals for biomedical applications. Prog Biomater. 2018;7:93–110. https://doi.org/10.1007/s40204-018-0091-4.

[15] Mandal S, Ummadi R, Bose M, Balla VK, Roy M. Fe–Mn–Cu alloy as biodegradable material with enhanced antimicrobial properties. Mater Lett. 2019;237:323–7. https://doi.org/10.1016/j.matlet.2018.11.117.

[16] Ma Z, Gao M, Na D, Li Y, Tan L, Yang K. Study on a biodegradable antibacterial Fe-Mn-C-Cu alloy as urinary implant material. Mater Sci Eng C. 2019;103:109718. https://doi.org/10.1016/j.msec.2019.05.003.

[17] Peuster M, Hesse C, Schloo T, Fink C, Beerbaum P, von Schnakenburg C. Long-term biocompatibility of a corrodible peripheral iron stent in the porcine descending aorta. Biomaterials. 2006;27:4955–62. https://doi.org/10.1016/j.biomaterials.2006.05.029.

[18] Ali S, Rani AM, Baig Z, Ahmed SW, Hussain G, Subramaniam K, et al. Biocompatibility and corrosion resistance of metallic biomaterials. Corros Rev. 2020;38:381–402. https://doi.org/10.1515/corrrev-2020-0001.

[19] Vojtěch D, Kubasek J, Capek J, Michalcova A, Pospíšilová I. Corrosion and mechanical behavior of biodegradable metallic biomaterials. Solid State Phenom. 2015;227:431–34. https://doi.org/10.4028/www.scientific.net/SSP.227.431.

[20] Kraus T, Moszner F, Fischerauer S, Fiedler M, Martinelli E, Eichler J, et al. Biodegradable Fe-based alloys for use in osteosynthesis: outcome of an in vivo study after 52 weeks. Acta Biomater. 2014;10:3346–53. https://doi.org/10.1016/j.actbio.2014.04.007.

[21] Lin W, Qin L, Qi H, Zhang D, Zhang G, Gao R, et al. Long-term in vivo corrosion behavior, biocompatibility and bioresorption mechanism of a bioresorbable nitrided iron scaffold. Acta Biomater. 2017;54:454–68. https://doi.org/10.1016/j.actbio.2017.03.020.

[22] Drynda A, Hassel T, Bach FW, Peuster M. In vitro and in vivo corrosion properties of new iron–manganese alloys designed for cardiovascular applications. J Biomed Mater Res Part B. 2015;103:649–60. https://doi.org/10.1002/jbm.b.33234.

[23] Dehestani M, Adolfsson E, Stanciu LA. Mechanical properties and corrosion behavior of powder metallurgy iron-hydroxyapatite composites for biodegradable implant applications. Mater Des. 2016;109:556–69. https://doi.org/10.1016/j.matdes.2016.07.092.

[24] Schinhammer M, Steiger P, Moszner F, Löffler JF, Uggowitzer PJ. Degradation performance of biodegradable FeMnC (Pd) alloys. Mater Sci Eng C. 2013;33:1882–93. https://doi.org/10.1016/j.msec.2012.10.013.

[25] Hufenbach J, Wendrock H, Kochta F, Kühn U, Gebert A. Novel biodegradable Fe-Mn-C-S alloy with superior mechanical and corrosion properties. Mater Lett. 2017;186:330–3. https://doi.org/10.1016/J.MATLET.2016.10.037.

[26] Liu B, Zheng YF, Ruan L. In vitro investigation of Fe30Mn6Si shape memory alloy as potential biodegradable metallic material. Mater Lett. 2011;65:540–3. https://doi.org/10.1016/j.matlet.2010.10.068.

[27] Hermawan H, Dubé D, Mantovani D. Degradable metallic biomaterials: design and development of Fe–Mn alloys for stents. J Biomed Mater Res Part A. 2010;93:1–11. https://doi.org/10.1002/jbm.a.32224.

[28] Liu B, Zheng YF. Effects of alloying elements (Mn, Co, Al, W, Sn, B, C and S) on biodegradability and in vitro biocompatibility of pure iron. Acta Biomater. 2011;7:1407–20. https://doi.org/10.1016/j.actbio.2010.11.001.

[29] Sotoudehbagha P, Sheibani S, Khakbiz M, Ebrahimi-Barough S, Hermawan H. Novel antibacterial biodegradable Fe-Mn-Ag alloys produced by mechanical alloying. Mater Sci Eng C. 2018;88:88–94. https://doi.org/10.1016/j.msec.2018.03.005.

[30] Safaie N, Khakbiz M, Sheibani S, Bagha PS. Synthesizing of nanostructured Fe-Mn alloys by mechanical alloying process. Procedia Mater Sci. 2015;11:381–5. https://doi.org/10.1016/j.mspro.2015.11.134.

[31] Bagha PS, Khakbiz M, Safaie N, Sheibani S, Ebrahimi-Barough S. Effect of high energy ball milling on the properties of biodegradable nanostructured Fe-35 wt.% Mn alloy. J Alloys Compd. 2018;768:166–75. https://doi.org/10.1016/j.jallcom.2018.07.261.

[32] Sivasankaran S, Sivaprasad K, Narayanasamy R, Iyer VK. An investigation on flowability and compressibility of AA 6061100-x-x wt.% TiO2 micro and nanocomposite powder prepared by blending and mechanical alloying. Powder Technol. 2010;201:70–82. https://doi.org/10.1016/j.powtec.2010.03.013.

[33] Sánchez F, Bolarín AM, Molera P, Mendoza JE, Ocampo M. Relationship between particle size and manufacturing processing and sintered characteristics of iron powders. Rev Latinoam Metal Mater. 2003;23:35–40.

[34] Ammar HR, Sivasankaran S, Alaboodi AS. Investigation of the microstructure and compressibility of biodegradable Fe–Mn–Cu/W/Co nanostructured alloy powders synthesized by mechanical alloying. Materials. 2021;14:1–23. https://doi.org/10.3390/ma14113088.

[35] Ammar HR, Sivasankaran S, Alaboodi AS, Al-Mufadi FA. Synthesis, microstructural investigation and compaction behavior of $Al_{0.3}CrFeNiCo_{0.3}Si_{0.4}$ nanocrystalline high entropy alloy. Adv Powder Technol. 2021;32:398–412. https://doi.org/10.1016/j.apt.2020.12.016.

[36] Ming QY, He LY. Powder-suspension dielectric fluid for EDM. J Mater Process Technol. 1995;52:44–54. https://doi.org/10.1016/0924-0136(94)01442-4.

[37] Montgomery DC. Design and analysis of experiments. 4th ed.New York, USA: Wiley; 1997. pp. 65–138.

[38] Sivasankaran S, Sivaprasad K, Narayanasamy R, Satyanarayana PV. X-ray peak broadening analysis of AA 6061_{100-x}- x wt.% Al_2O_3 nanocomposite prepared by mechanical alloying. Mater Charact. 2011;62:661–72. https://doi.org/10.1016/j.matchar.2011.04.017.

[39] Sivasankaran S. Optimization on dry sliding wear behavior of yellow brass using face centered composite design. AIMS Mater Sci. 2019;6:80–96. https://doi.org/10.3934/matersci.2019.1.80.

[40] Sivasankaran S, Ramkumar KR, Al-Mufadi FA, Irfan OM. Effect of TiB2/Gr hybrid reinforcements in Al 7075 matrix on sliding wear behavior analyzed by response surface methodology. Met Mater Int. 2021;27:1739–55. https://doi.org/10.1007/s12540-019-00543-5.

Received 2021-09-23
Accepted 2021-11-21